metals

MDPI

Article

Corrosion Behavior and Microhardness of a New B_4C Ceramic Doped with 3% Volume High-Entropy Alloy in an Aggressive Environment

Alberto Daniel Rico-Cano [1], Julia Claudia Mirza-Rosca [1,2,*], Burak Cagri Ocak [3] and Gultekin Goller [3]

[1] Departament of Mechanical Engineering, University of Las Palmas de Gran Canaria, Campus Universitario Tafira, 35017 Las Palmas de Gran Canaria, Spain; alberto.rico101@alu.ulpgc.es
[2] Materials Engineering and Welding Department, Transilvania University of Brasov, 500036 Brasov, Romania
[3] Department of Metallurgical and Materials Engineering, Istanbul Technical University, 34469 Maslak, Istanbul, Turkey; ocakb@itu.edu.tr (B.C.O.); goller@itu.edu.tr (G.G.)
* Correspondence: julia.mirza@ulpgc.es

Abstract: The aim of this paper is to study both the mechanical and chemical properties of a new material composed of B_4C doped with 3% volume of CoCrFeNiMo HEA by the spark plasma sintering technique. Scanning electron microscopy and microhardness were used to characterize the composite microstructure and hardness. Corrosion behavior was studied by corrosion potential, corrosion rate and electrochemical impedance spectroscopy, where the equivalent circuit was obtained, characterized by the presence of the Warburg element. The addition of HEA resulted in a more compact microstructure, filling pores and inhibiting ceramic grain growth. A microhardness statistical analysis revealed that the sample followed a normal distribution, which suggests that the sample has a homogeneous structure. The doped material exhibits excellent corrosion resistance in artificial seawater, where its chemical interaction occurs in two steps, with an important diffusional component. This study highlights the potential for use in environments where both corrosion resistance and mechanical strength are critical factors.

Keywords: ceramic; HEA; EIS; corrosion behavior; microhardness; SEM

Academic Editor: Thomas Fiedler

Received: 28 November 2024
Revised: 9 January 2025
Accepted: 15 January 2025
Published: 17 January 2025

Citation: Rico-Cano, A.D.; Mirza-Rosca, J.C.; Ocak, B.C.; Goller, G. Corrosion Behavior and Microhardness of a New B_4C Ceramic Doped with 3% Volume High-Entropy Alloy in an Aggressive Environment. *Metals* **2025**, *15*, 79. https://doi.org/10.3390/met15010079

1. Introduction

Boron carbide (B_4C) possesses a distinctive combination of characteristics that make it a preferred material for various technical applications. Boron carbide is utilized in refractory applications owing to its elevated melting point (2450 °C) and thermal stability and conductivity (30 W/m K). It serves as an abrasive powder and coating due to its exceptional abrasion resistance. Its elevated hardness renders it appropriate for grinding and cutting tools, ceramic bearings, wire drawing dies, and similar applications. It demonstrates superior ballistic performance due to its high hardness (30 GPa) and low density (2.52 g/cm^3). Boron carbide is an exceptional thermoelectric material due to its elevated Seebeck coefficient of 300 μV K^{-1}, and novel uses in thermocouples, diodes, and transistor devices are being discovered [1]. B_4C is extremely hard, ranked third after diamond and cubic boron nitride. B_4C has lower density, making it lightweight compared with diamond, which has higher density (~3.51 g/cm^3). Boron carbide is a good thermal conductor, though not as high as diamond that has exceptional thermal conductivity, the highest among known materials. B_4C is generally a semiconductor with low electrical conductivity, while diamond is an excellent electrical insulator; however, doped diamonds can exhibit semiconducting properties. B_4C is highly resistant to chemical corrosion, making it suitable

for harsh environments, while diamond is chemically inert and resistant to most acids and alkalis but can be oxidized at high temperatures. B_4C is less expensive and more readily available in large quantities for industrial applications [1].

In medicine, ionizing radiation is essential for diagnostic imaging techniques, including X-rays, CT scans, and nuclear medicine treatments. In industrial applications, radiation is employed in sterilizing, material testing, and quality control, thereby improving safety and efficiency. Furthermore, electricity generation by nuclear power constitutes a significant share of global energy output, offering a low-carbon alternative to traditional fossil fuels. The difficulty resides in utilizing the advantages of ionizing radiation while limiting the related dangers. Under these conditions, shielding is an essential element in radiation protection measures, and boron carbide possesses significant neutron absorption capacity (600 barns). B_4C ceramics are extensively utilized in nuclear applications, such as the protection and supervision of nuclear reactors [2,3].

Moreover, B_4C exhibits superior hardness and reduced density in comparison to ceramic materials such as Al_2O_3, ZrO_2, SiC, and Si_3N_4. Boron carbide-reinforced polymer composites are increasingly being recognized for tribological applications that necessitate low friction and minimal wear [4].

Boron carbide is a semiconductor characterized by hopping-type electrical transport features. The energy band gap is dependent on composition and the extent of order. Reports indicate a band gap of 2.09 eV, which includes several mid-bandgap states that complicate the photoluminescence spectra. The material is generally p-type with potential uses in innovative electronic devices [5].

The densification of boron carbide is crucial due to the necessity for dense bodies in many specific applications. Numerous sinter additives have been evaluated for their ability to increase the rate of densification, control grain development, and improve the mechanical characteristics of boron carbide. Carbon has been highly useful in decreasing the oxide layer of boron carbide powders, hence facilitating sintering and inhibiting grain development [6]. The same authors conducted a systematic study on the effects of the addition of the same weight percent of different sintering additives (C, B, TiB2, and CSi) on the density, hardness and wear resistance of B_4C compacts, produced by pressureless sintering.

Many research efforts have been undertaken to improve the fracture toughness and mechanical properties of B_4C ceramics through the incorporation of metallic sintering additives such as Co [7], Fe [8,9], Si [10], Ti [11], and Ni [12].

While the reduction in sintering temperature has been documented with the incorporation of metallic aids, these metals may result in diminished hardness values. Considering the aforementioned factors, a novel strategy may be implemented to tackle these challenges with the incorporation of HEAs as sintering additives.

HEAs, or high-entropy alloys, are a relatively new family of materials, characterized by the inclusion of at least five different metallic elements in nearly equal atomic ratios, unlike traditional alloys, which typically consist of only one or two primary elements [13]. HEAs possess remarkable properties, such as excellent corrosion resistance, high strength, and impressive ductility and stability at elevated temperatures, which have captured the interest of the scientific community [14]. Potential applications for HEAs include energy systems [15,16], nuclear technology [17,18], and biomedical fields [19,20].

Doping high-entropy alloys (HEAs) involves the deliberate introduction of small amounts of additional chemical elements into the base alloy composition [21]. This process can significantly impact the alloy's mechanical and physical properties. The impact of doping is primarily influenced by the types of elements introduced, their concentrations, and the specific application intended for the alloy. By strategically adjusting the doping

process, HEAs can be tailored to possess properties that meet the requirements of particular operating conditions.

CoCrFeNiMo HEA has been used as coating on 304 stainless steel [22–24] and 316 stainless steel [25] or doped with other metals such as titanium [14], zirconium [26], and aluminum [27]. The inclusion of Cr and Ni significantly enhances the corrosion resistance of the FeNiCoCrMo high-entropy alloy (HEA) by forming a dense, protective oxide layer over the substrate [28,29]. Additionally, Mo, with its high melting point [30,31], contributes to the formation of Mo-rich phases, imparting higher hardness and reducing pitting corrosion due to lattice distortion [32]. In previous studies, the effects of varying Mo concentrations (CoCrFeNiMox, $x \leq 0.25$) on the corrosion resistance of HEA coatings in acidic environments, such as 3.5 wt% NaCl solutions, have been explored, concluding that the passivation film, composed mainly of Cr_2O_3 and MoO_3, was the key factor in enhancing the corrosion resistance [25]. In similar studies it was demonstrated that the formation of a passivation film in CoCr2FeNiMox ($x \leq 0.4$) coatings improved corrosion resistance in acidic 3.5 wt% NaCl solutions [33].

In this context, combining CoCrFeNiMo HEA with B_4C as a composite seeks to benefit from the remarkable mechanical strength and corrosion resistance offered by the HEA while utilizing the high hardness and thermal stability of B_4C.

Thus, in this study, the corrosion behavior of a novel B_4C ceramic material doped with CoCrFeNiMo HEA is investigated to assess its performance in an artificial seawater environment—a 3.5% in volume NaCl solution. In addition to corrosion testing, this study aims to conduct a statistical analysis of the microhardness behavior of the material. This research aims to assess the potential of these materials for use in harsh and corrosive environments, with a particular focus on applications where durability, corrosion resistance, and improved hardness are critical factors.

2. Materials and Methods

2.1. Material Preparation

This investigation focused on a B_4C ceramic sample doped with 3 vol.% CoCrFeNiMo HEA. This material was synthesized at Istanbul Technical University by the Department of Metallurgical and Materials Engineering. First, the starting powders were weighed accurately and mixed for 6 h using a tubular mixer (T2F Bachofen, Bachofen AG, Muttenz, Switzerland) to ensure homogeneity. The mixed powders were then placed into a hollow graphite die with an inner diameter of 50 mm and a thickness of 4 mm. To enhance electrical and thermal conductivity and facilitate easy removal after sintering, a graphite sheet was inserted between the punches and the powder. Additionally, the graphite die was insulated with carbon felt to minimize heat loss.

The sintering process was conducted in a vacuum atmosphere using an SPS apparatus (SPS-7.40 MK-VII, SPS Syntex Inc., Saitama, Japan). A pulsed direct current (12 ms/on, 2 ms/off) and uniaxial pressure of 40 MPa were applied throughout the process. The temperature was monitored with an optical pyrometer (Chino, IR-AH, Tokyo, Japan) capable of measuring temperatures above 570 °C, focusing on a small hole in the graphite die. The process was temperature-controlled, and the shrinkage behavior of the samples was tracked continuously via punch rod displacement. To account for the thermal expansion of the graphite punches, a blank test was conducted, and the expansion values were subtracted from the measured shrinkage data.

The optimized SPS parameters were set as follows: sintering temperature of 1600 °C, heating rate of 100 °C/min, and a holding time of 5 min. The final samples had a diameter of 50 mm and a thickness of 4 mm.

Before performing mechanical and electrochemical tests, the ingot was embedded in two-component epoxy resin for easier handling. The sample was then polished in two stages using a Struers TegraPol-11 (Copenhague, Denmark) polisher: first, with silicon carbide abrasive papers (from 240 to 2000 grit) and later with a 0.1 µm alpha alumina suspension to achieve a mirror-like finish. The whole manufacturing of the sample and preparation process is illustrated in Figure 1.

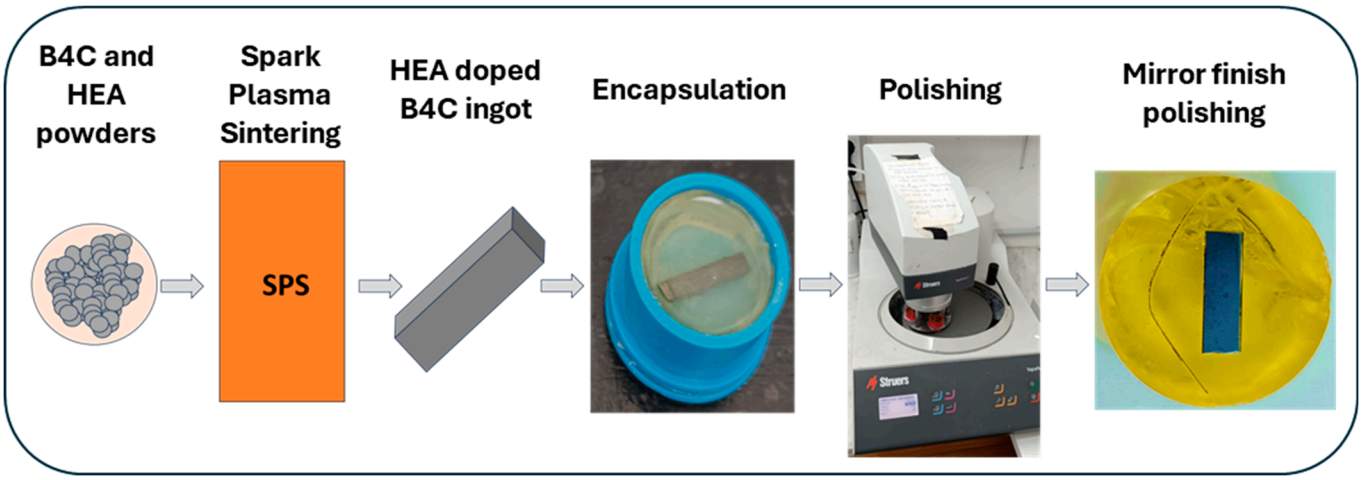

Figure 1. Schematic representation of the material preparation.

2.2. Scanning Electron Microscopy (SEM)

The microstructure of the sintered sample was analyzed through scanning electron microscopy model, FESEM JSM 7000 F (JEOL Ltd., Tokyo, Japan). To visualize effectively the microstructural features and facilitate the interpretation of the results obtained, the samples were etched using an electrolytic process to reveal the grain boundaries, employing a 10% NaOH solution for 15 s under conditions of 10 V and a current density of 0.25 A/cm^2.

2.3. Electrochemical Tests

After sample preparation, three different electrochemical tests were conducted using a BioLogic Essential SP-150 potentiostat (Bio-Logic Science Instruments SAS, Seyssinet-Pariset, France) and an electrochemical cell. These tests included open circuit potential (OCP), linear polarization, and electrochemical impedance spectroscopy (EIS) in an acidic environment—a 3.5% NaCl artificial seawater solution. The EC-Lab® v-9.55 software was used to set test parameters and analyze the results, following the ASTM G5-94(2004) standard [34]. The conventional electrochemical cell had three electrodes: the doped B_4C as the working electrode, a saturated calomel reference electrode, and a platinum counter electrode.

2.3.1. Corrosion Potential

Using the "Ecorr vs. Time" technique, for 24 h, the open circuit potential of the sample was recorded, with measurements taken every 30 s or when a 100 mV change in potential occurred. To determine whether the sample's corrosion potential remained stable, indicated passivation, or showed signs of corrosion over time, the recorded data were plotted.

2.3.2. Corrosion Rate

For linear polarization measurements, the sample's potential was stabilized by inputting the surface area and test duration (110 min). The potential was scanned at a rate of 10 mV/min, ranging from −0.1 to 1 V versus the open circuit potential. The resulting data were used to generate polarization curves, and the corrosion rate of the sample was calculated using the EC-Lab's "Tafel Fit" technique.

2.3.3. EIS

EIS, or electrochemical impedance spectroscopy, is a nondestructive test and was used to measure the sample's electrochemical impedance by applying an alternating current to the electrochemical cell at different frequencies and recording the resulting current. The test followed the ISO 16773-1-4:2016 standard [35]. To visualize the collected data, Nyquist and Bode diagrams were used. For further analysis and to simulate the electrochemical behavior of the materials, equivalent circuits (EC) were applied. These circuits helped in accurately modeling and understanding the complex impedance characteristics observed during the tests.

2.4. Microhardness

The Vickers microhardness of the sample was evaluated using an indentation test on a FM-810 Microhardness Tester (Future Tech, Kawasaki, Japan). The surface was polished to a mirror finish to ensure clear visibility of the indentation marks. Indentations were made with a prudent distance between them to avoid interference with the measurements. The test was conducted following the ISO 14577-1:2015 standard [36]. However, due to the high hardness of the material, a load of 2 kgf was applied to measure the indentation marks accurately. A total of 45 indentations were made on different regions of both the monolithic and doped B_4C samples, and the average Vickers hardness (HV_2) value was then calculated.

3. Results and Discussion

3.1. Scanning Electron Microscope (SEM)

Figure 2 shows, at low and high-magnification (3500× and 5000×), how a much denser microstructure is obtained by adding CoCrFeNiMo HEA to monolithic B_4C, as theoretical density suggested (monolithic B_4C: 2.52 g/cm^3; 3% HEA B_4C: 2.71 g/cm^3) and measured density corroborated (monolithic B_4C: 2.43 g/cm^3; 3% HEA B_4C: 2.66 g/cm^3) [37].

According to German et al. [38], liquid phases naturally tend to occupy configurations with the lowest energy, preferentially flowing into pores or smaller grains. This behavior, combined with the presence of CoCrFeNiMo HEA phases at triple junctions and grain boundaries, inhibits grain growth and results in finer grains. For instance, the microstructure of the 3% B_4C HEA demonstrates only a slight reduction in grain size (2.52 μm) compared to monolithic B_4C (2.57 μm) [37].

3.2. Electrochemical Tests

3.2.1. Corrosion Potential

The corrosion potential indicates the voltage at which the cathodic current density shifts to anodic when a metal is immersed in a solution. In accordance with the Mixed Potential Theory proposed by Wagner and Traud [39], oxidation and reduction reactions involved in corrosion occur at equal rates on the metal's surface. The change in corrosion potential as time passes serves as an accurate measure of corrosion behavior, although it is not sufficient for a comprehensive analysis.

In our observations, the corrosion potential of the sample first decreased but rapidly increased in two steps with the immersion time, indicating that the sample became passivated in the solution. The curve did not display any potential drops that would typically be inherent in surface activation during exposure to the corrosive solution, which implies that the passive film of the outer layers is thermodynamically stable under these conditions (see Figure 3).

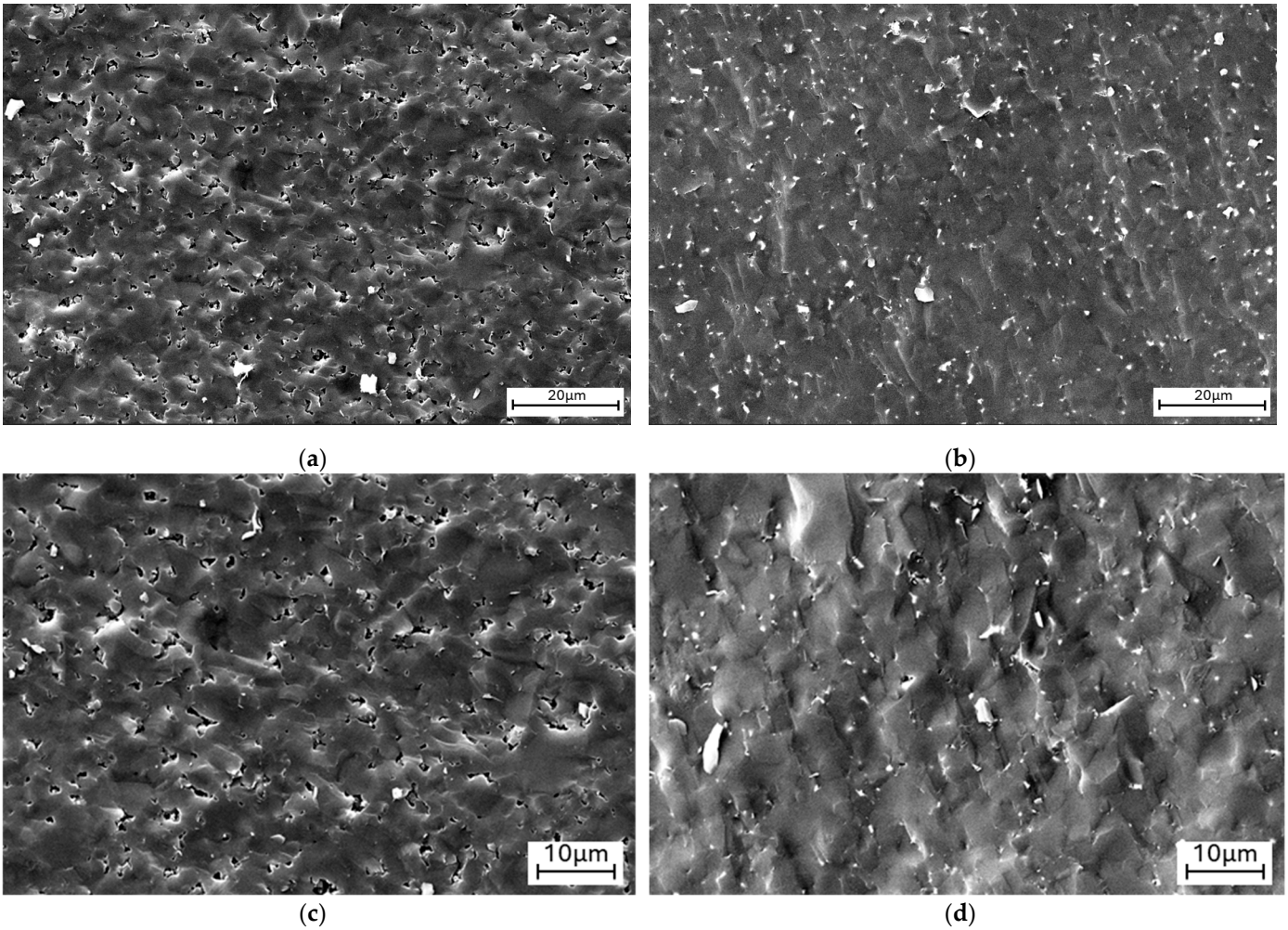

Figure 2. SEM images of (**a**) monolithic B_4C at 3500× magnification, (**b**) 3% HEA-doped B_4C at 3500× magnification, (**c**) monolithic B_4C at 5000× magnification, and (**d**) 3% HEA-doped B_4C at 5000× magnification.

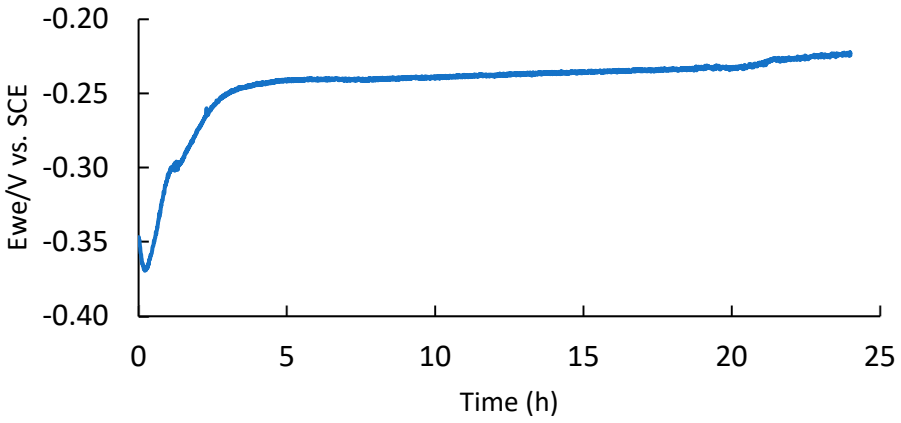

Figure 3. Corrosion potential vs. time for 24 h of immersion in 3.5% NaCl solution.

3.2.2. Corrosion Rate

It was found that liquid phases [38] generally favor the lowest energy configuration, causing them to move preferentially toward smaller grains and pores, which helps account for the observed linear polarization behavior (see Figure 4).

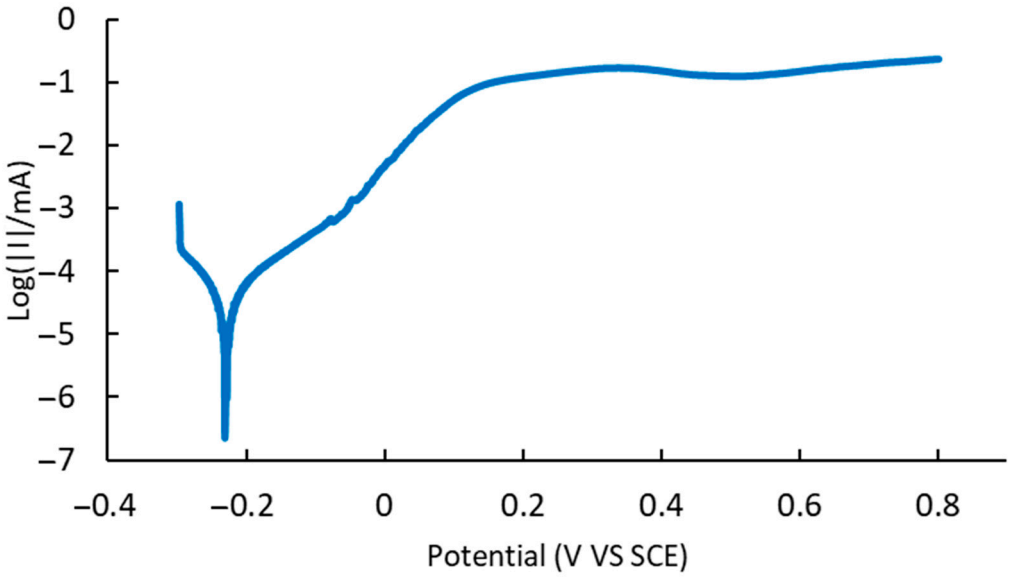

Figure 4. Polarization curve of B_4C 3% HEA-doped sample in 3.5% NaCl solution.

3.2.3. Electrochemical Impedance Spectroscopy (EIS)

This advanced technique is particularly useful for investigating the interfacial characteristics related to processes occurring on the surfaces of metallic alloys. Compared to other electrochemical methods, EIS offers several advantages, as it operates in a stationary state, measuring small signals effectively and is capable of probing frequencies ranging from 100 mHz to 100 kHz.

The selection of a frequency range from 100 mHz to 100 kHz for electrochemical impedance spectroscopy (EIS) measurements is driven by the necessity to encompass a broad spectrum of electrochemical processes and system characteristics. The high frequency ranges (10 kHz to 100 kHz) allow for the capture of information pertaining to the bulk properties of the electrolyte, including ionic conductivity. This also illustrates the high-frequency response of the system, including capacitive behaviors and dielectric properties. The mid frequencies range (1 Hz to 10 kHz) offers valuable insights into charge transfer resistance and double-layer capacitance, helping in the comprehension of processes such as ion diffusion and interfacial phenomena at the electrode/electrolyte interface. The low frequencies range (100 mHz to 1 Hz) indicates slow processes such as diffusion (Warburg impedance) and long-term stability, playing a vital role in analyzing phenomena like mass transport limitations, electrode porosity, and faradaic reactions.

Frequencies below 100 mHz are typically avoided because of the considerable time needed for stable measurements and the possibility of noise interference. Frequencies exceeding 100 kHz are unlikely to provide substantial additional helpful data for numerous electrochemical systems and were also constrained by the limitations of our equipment's capabilities.

Bode and Nyquist Diagrams in 3.5% NaCl Solution

The results from electrochemical impedance spectroscopy are displayed in Bode phase impedance plots, recorded at the same potential in a 3.5% NaCl solution. The highest impedance value was 60.047 kΩ, and the maximum phase angle was 70.5° (see Figure 5). The electrochemical impedance spectroscopy data collected showed incredibly high resistance to corrosion in a 3.5% NaCl solution.

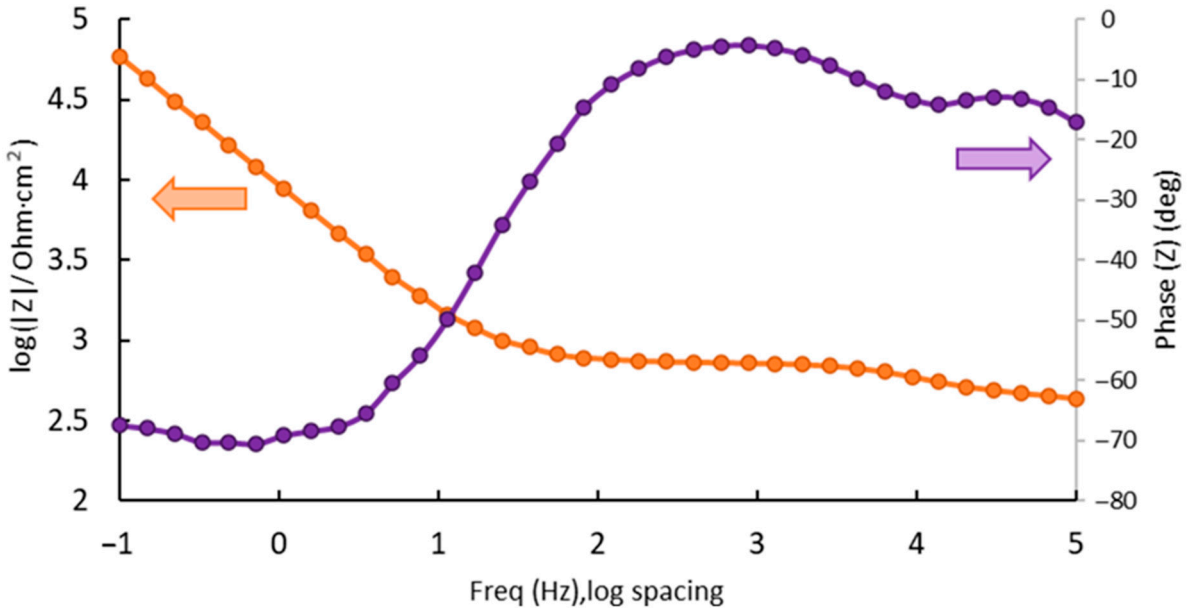

Figure 5. Bode-IZI and Bode phase for doped samples at Ecorr after 24 h of immersion in 3.5% NaCl solution.

The Nyquist diagram (see Figure 6) depicts three zones: high frequencies describe one semicircle, a second semicircle is described at medium frequencies, and finally at high frequencies, a straight line revealing diffusion appears. The behavior is determined by a two stages process: first, the filling of the pores and cracks with a 3.5% NaCl solution (with a remarkable diffusional component), followed by the creation of a passive film within those pores and on the material's surface. Similar results were obtained with B_4C doped with 2% CoCrFeNiMo HEA [40].

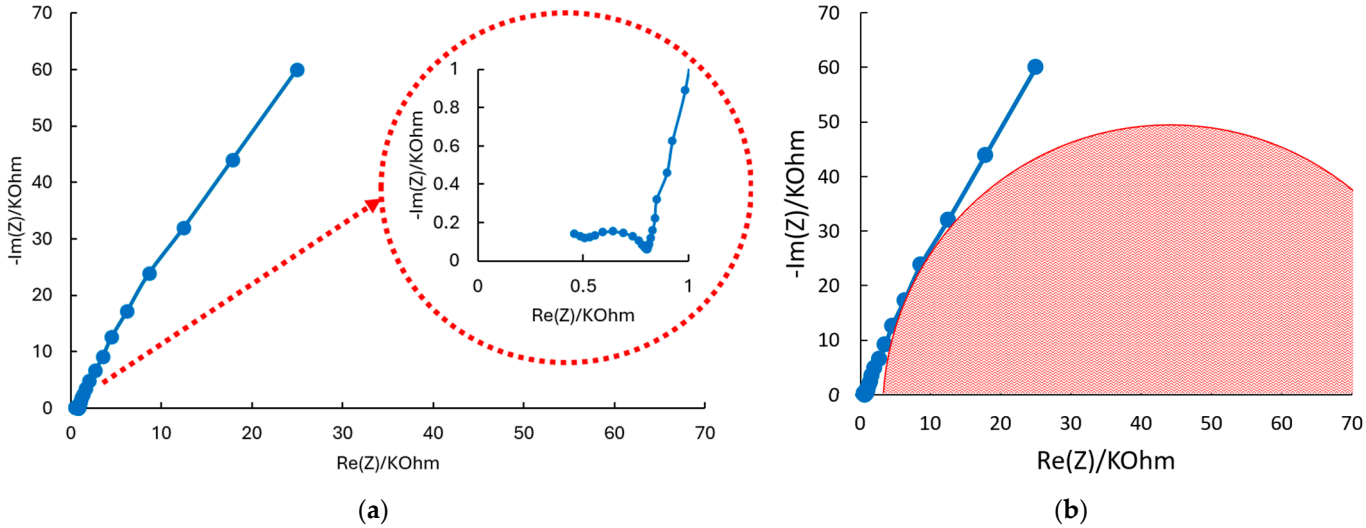

Figure 6. Nyquist diagrams for doped samples at Ecorr after 24 h of immersion in 3.5% NaCl solution with (**a**) higher detail at low frequencies and (**b**) higher detail at medium frequencies.

The equivalent circuit model R(Q(R(QR)Q(RW))), which most accurately aligns with the experimental results for sample B_4C 3% HEA, is illustrated in Figure 7. This circuit indicates that until the alloy film is reached, the outer layer of the sample demonstrates dissolution resistance, featuring a both porous and dense passive layer.

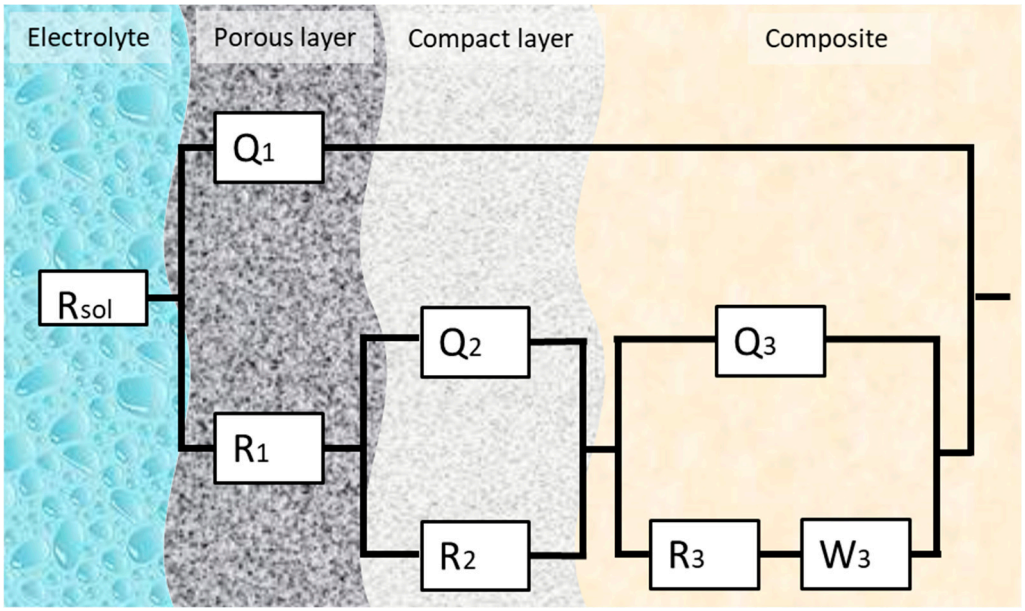

Figure 7. Equivalent circuit R(Q(R(QR)Q(RW))).

The electrical equivalent circuit was employed to model the experimental EIS data. The impedance spectra were processed by using the software ZSimpWin 3.6 (Informer Technologies, Los Angeles, CA, USA). The accuracy of the fit was determined by comparing the simulated results with the experimental data collected, where the chi-square value is calculated. A chi-square value near 10^{-5} indicates a highly precise fit with only a few components required for the model [41].

The formula obtained by applying Kirchhoff's circuit laws to this new circuit is as follows:

$$Z_{circuit} = R_{sol} + \frac{1}{\frac{1}{Q_1} + \frac{1}{R_1 + \frac{1}{\frac{1}{R_2}+\frac{1}{Q_2}} + \frac{1}{\frac{1}{R_3+W_3}+\frac{1}{Q_3}}}} \quad (1)$$

After obtaining Equation (1), it is simplified to yield the following equation:

$$Z_{circuit} = R_{sol} + \frac{Q_1 \cdot \left(R_1 + \frac{R_2 \cdot Q_2}{R_2+Q_2} + \frac{(R_3+W_3)\cdot Q_3}{(R_3+W_3)+Q_3}\right)}{Q_1 + R_1 + \frac{R_2 \cdot Q_2}{R_2+Q_2} + \frac{(R_3+W_3)\cdot Q_3}{(R_3+W_3)+Q_3}} \quad (2)$$

The letter "Q" stands for a constant phase element (CPE).It is normally used when the impedance data are not adequate for basic circuits elements and therefore, allow for the consideration of the passivated surface. The impedance provided by a CPE is described by the following equation [41]:

$$Z_{CPE} = \frac{1}{Y_0(jw)^n} \quad (3)$$

The letter "W" on the equivalent circuit stands for the Warburg element, which represents the movement or diffusion of electrons or ions in solid or liquid phases. It is represented by the following equation [42]:

$$Z_W = \frac{1}{Y_0(jw)^{0.5}} \quad (4)$$

Replacing the Equation (2) Warburg element and the constant phase elements, we create the following equation for the equivalent circuit obtained:

$$Z_{circuit} = R_{sol} + \frac{\frac{1}{Y_1(jw)^{n_1}} \cdot \left[R_1 + \frac{R_2 \cdot \frac{1}{Y_2(jw)^{n_2}}}{R_2 + \frac{1}{Y_2(jw)^{n_2}}} + \frac{\left(R_3 + \frac{1}{Y_W(jw)^{0.5}} \right) \cdot \frac{1}{Y_3(jw)^{n_3}}}{\left(R_3 + \frac{1}{Y_W(jw)^{0.5}} \right) + \frac{1}{Y_3(jw)^{n_3}}} \right]}{\frac{1}{Y_1(jw)^{n_1}} + R_1 + \frac{R_2 \cdot \frac{1}{Y_2(jw)^{n_2}}}{R_2 + \frac{1}{Y_2(jw)^{n_2}}} + \frac{\left(R_3 + \frac{1}{Y_W(jw)^{0.5}} \right) \cdot \frac{1}{Y_3(jw)^{n_3}}}{\left(R_3 + \frac{1}{Y_W(jw)^{0.5}} \right) + \frac{1}{Y_3(jw)^{n_3}}}} \quad (5)$$

Table 1 shows the circuit equivalent parameters for the sample under study.

Table 1. R(Q(R(QR)Q(RW))) circuit equivalent parameters for B_4C doped sample.

Parameters	Results
Y_1 ($S \cdot sec^n/cm^2$)	$1.001 \cdot 10^{-8}$
n_1	0.856
R_1 ($ohm \cdot cm^2$)	378.6
Y_2 ($S \cdot sec^n/cm^2$)	$1.226 \cdot 10^{-7}$
n_2	0.968
R_2 ($ohm \cdot cm^2$)	209.8
Y_3 ($S \cdot sec^n/cm^2$)	$2.061 \cdot 10^{-5}$
n_3	0.894
R_3 ($ohm \cdot cm^2$)	6363
Y_W ($S \cdot sec^5/cm^2$)	$8.952 \cdot 10^{-6}$
Chi-square	$1.22 \cdot 10^{-4}$

This model captures the processes occurring in the outer and inner layers of the material during electrochemical testing, specifically in relation to its corrosion resistance and passive film characteristics. When observing a bi-layer passive film consisting of a porous layer in contact with the electrolyte and a compact layer in contact with the underlying metal sample, several key characteristics and mechanisms influence the film's performance, especially regarding diffusion and long-term corrosion resistance.

The porous outer layer exhibits greater permeability to ions and water from the electrolyte, potentially acting as a barrier while facilitating the entrance of hostile species, such as chloride ions, from the environment. Ions, such as corrosive chlorides, may pass through the porous outer layer, with the diffusion rate dependent upon the layer's porosity, thickness, and rugosity. Oxygen may also penetrate the porous layer, contributing to oxidation reactions at the interface of the compact layer.

The compact layer (inner layer) is dense and provides the main barrier by restricting ion and electron transit. It attaches firmly to the metal surface, offering a more efficient barrier against corrosion. The compact layer exhibits reduced permeability and serves as a principal defense mechanism by markedly impeding the diffusion of aggressive ions, resulting in decreasing the rate of metal dissolution. The integrity and stability of this layer are essential for prolonged corrosion resistance.

The diffusion process affects long-term corrosion resistance, since the persistent access of hostile ions through the porous layer might result in the localized degradation of the compact layer over time. The compromise of the compact layer may accelerate corrosion rates, resulting in pitting or crevice corrosion. The system's capacity to re-passivate by generating a new compact layer is essential for long-term resistance if the compact layer is compromised. The migration of metal ions (e.g., Fe^{2+}, Cr^{3+}) from the metal substrate to the outer layer can facilitate the development of protective oxides. Oxygen diffusion through the porous layer is essential for sustaining passivity by facilitating the creation and

repair of oxide layers; insufficient oxygen supply can impede the re-passivation process, increasing the danger of corrosion in low-oxygen environments.

The results obtained suggest multiple layers of corrosion products, from a porous outer film to a more compact intermediate layer, and capture the impedance characteristics of the alloy surface. The presence of Warburg impedance on the layer closer to the alloy suggests that diffusion plays a significant role in the corrosion dynamics, improving the protective properties of the HEA system.

3.3. Microhardness

This test involves applying a vertical load onto the surface of the sample under study. In this case, the B_4C sample doped with a 3% volume of HEA was compared to monolithic B_4C by using a 136° edge angle pyramidal tetrahedral indenter from the hardness tester. The process continues for 15 s until an indentation was formed and, according to the Vickers method, a relationship was established between the applied load and the two diagonal measurements that describe the area of the indentation.

When analyzing the results from this technique, it is important to consider that the SEM images showed a porous microstructure with cracks appearing along the grain boundaries related to the presence of agglomerated HEA phases on the grain unions, as was corroborated by the equivalent circuit obtained from the electrochemical tests [37].

For this study, Vickers hardness was calculated using a fixed load of 2 kgf, as lower loads were insufficient to indent the sample effectively. The Vickers hardness values of indentation on the B_4C sample doped with a 3% volume of HEA can be seen in Figure 8.

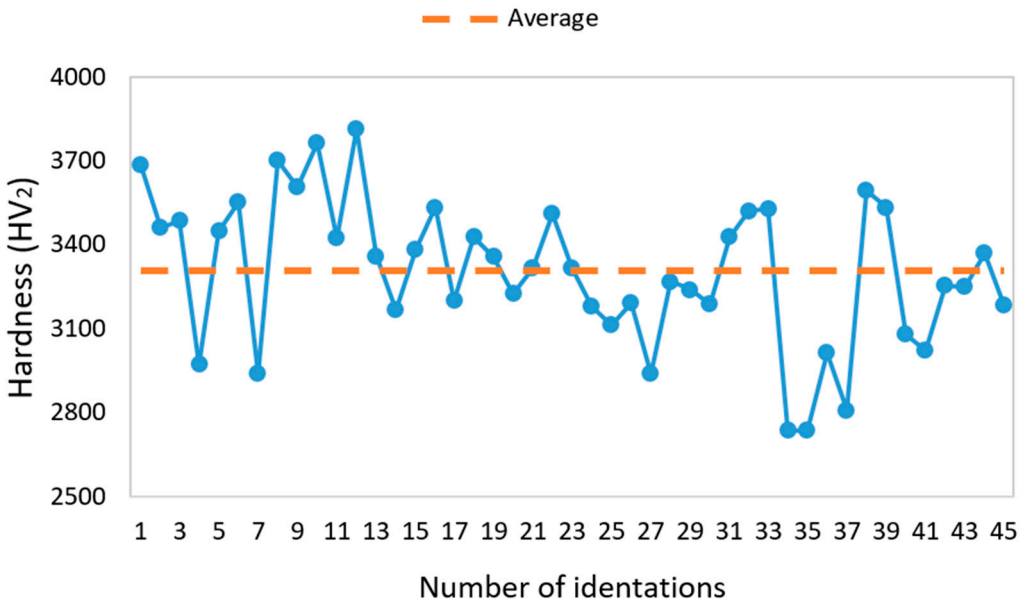

Figure 8. Microhardness values of each indentation for B_4C 3% HEA sample.

This variation can be attributed to the differing hardness levels of both the main phases seen in the SEM, B_4C and HEA, or the cracks noticed on the microstructure, as seen in other B_4C composite microhardness studies [43–45]. Therefore, a statistics study was applied to analyze and compare the distribution and variability of the Vickers hardness measurements of both samples. The results are summarized in Table 2, and various plots (boxplots, scatter plots, histograms, and normal distribution) are generated to visualize the distribution and comparison of hardness values across both samples (see Figure 9).

Table 2. Statistical parameters of Vickers hardness measurements for both B_4C doped and monolithic samples.

Statistical Parameter	Monolithic B_4C (HV_2)	Doped B_4C (HV_2)
Mean	2966.67	3308.57
Median	2990.0	3319.0
Standard Deviation	181.09	258.8
Minimum	2621.0	2737.0
Maximum	3381.0	3813.0
Quartile 25	2812.0	3182.0
Quartile 50 (Median)	2990.0	3319.0
Quartile 75	3074.0	3514.0

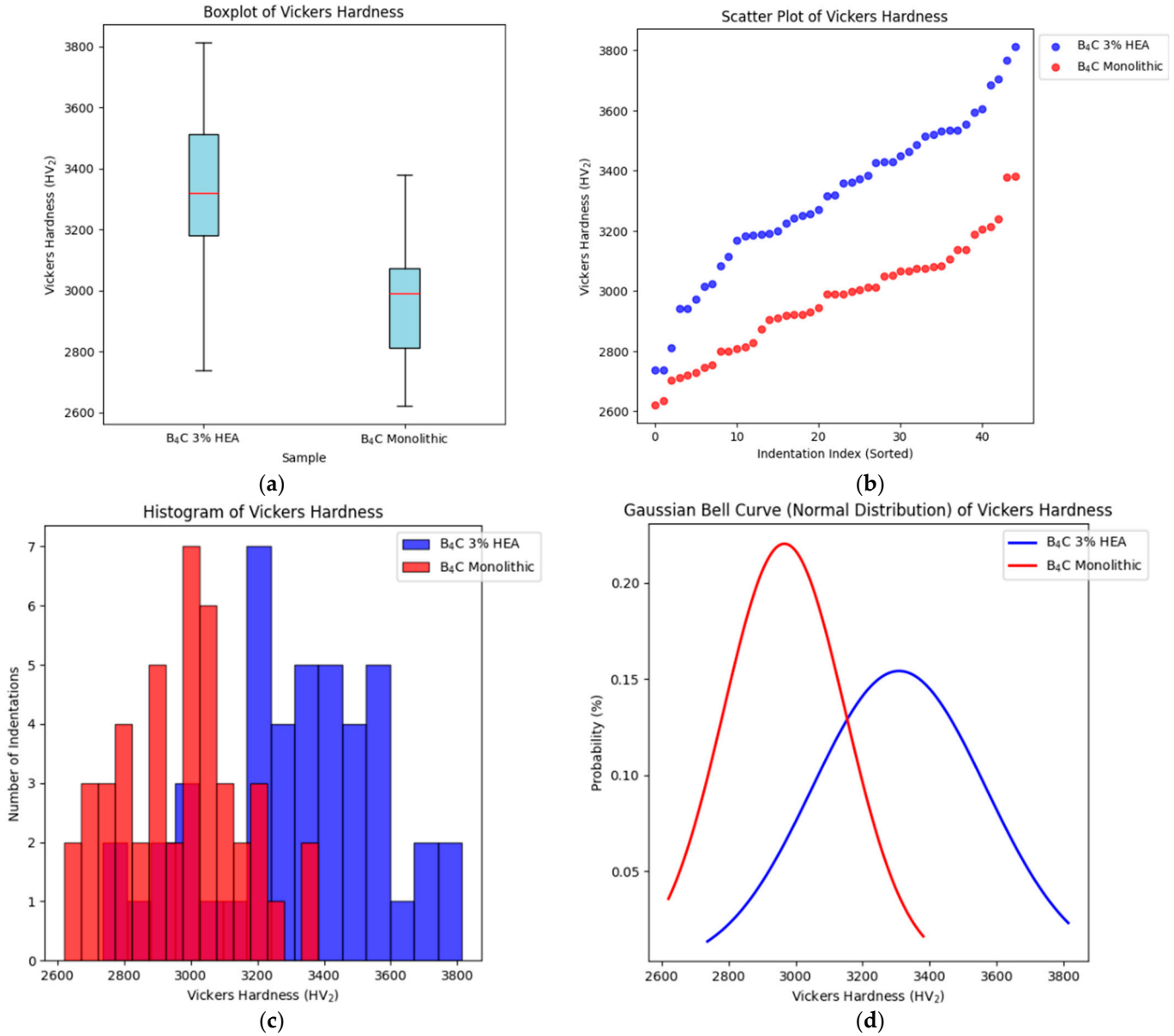

Figure 9. Vickers hardness for both B_4C monolithic and doped samples comparison: (**a**) distribution of Vickers hardness data through its quartiles; (**b**) dispersion of Vickers hardness values; (**c**) frequency of Vickers hardness values within certain intervals (bins); (**d**) probability distribution of the hardness values.

Through statistical analysis and the generated graphs, we can observe key trends in the hardness distribution of both samples. The B_4C doped sample results are harder than that of monolithic B_4C. Although there is a notable difference between the minimum and maximum values of both samples, most indentations are concentrated within a narrower range, especially in monolithic B_4C. This concentration suggests that both samples have a homogeneous structure and follow a normal distribution. The Vickers indentation led to radial cracks (see Figure 10), as seen in other B_4C composite studies [37,45].

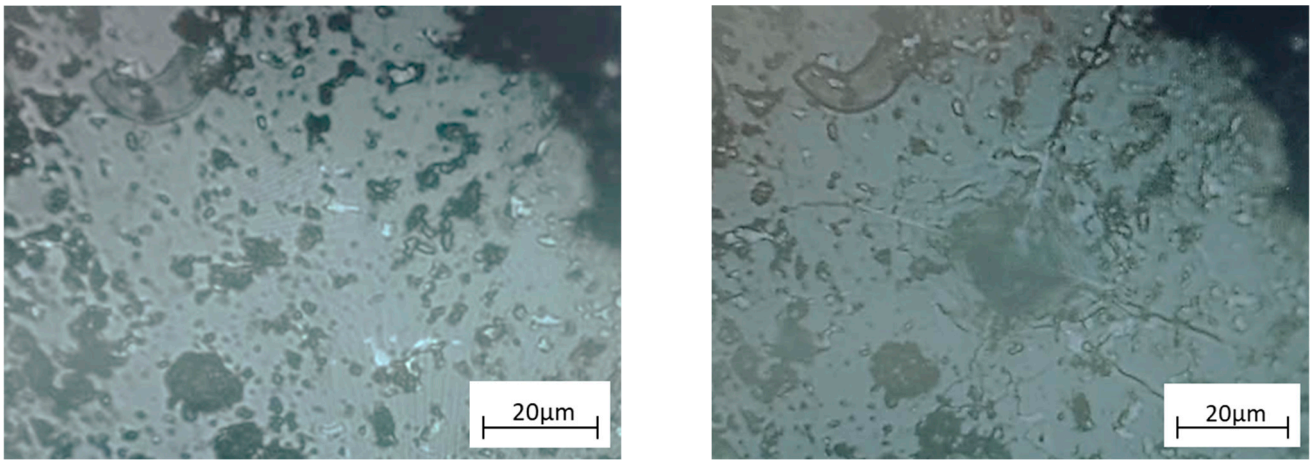

(**a**) (**b**)

Figure 10. B_4C doped sample (**a**) before Vickers indentation and (**b**) after Vicker indentation.

Densification leads to increased hardness as it results in a reduction of voids and defects within the microstructure. Increased density enhances the load-bearing capacity, as evidenced by the elevated microhardness values.

Hardness is influenced by grain boundary strengthening, as the increase in grain boundary area from grain refinement due to HEA doping leads to enhanced resistance and plastic deformation.

Secondary phases resulting from HEA doping can serve as reinforcement, thereby improving the overall strength and hardness of the material. The phases may also act to pin dislocations, thereby hindering plastic deformation and enhancing hardness.

The enhancement in microhardness resulting from the HEA doping of B_4C can be ascribed to improved densification, grain refinement, and the development of reinforcing secondary phases. The microstructural alterations decrease porosity, improve grain boundary strengthening, and obstruct dislocation movement, collectively leading to increased hardness values.

4. Conclusions

The behavior of 3% HEA B_4C ceramic in an artificial seawater environment was thoroughly investigated and the key findings can be summarized as follows:

- The addition of the CoCrFeMoNi high-entropy alloy to the B_4C ceramic significantly changed its microstructure, leading to a denser and more compact configuration when compared to undoped B_4C. This doping process effectively inhibited grain expansion, resulting in a more refined grain structure.
- The doped sample exhibited remarkable resistance to corrosion in the artificial seawater, making it suitable for applications in marine or corrosive environments conditions.
- The chemical reactions that occur when the doped sample was immersed in artificial seawater followed a two-step process, with a significant diffusional component involved. Initially, the seawater penetrated the material's surface, followed by the

formation of protective films or layers that prevent further degradation, contributing to the observed high corrosion resistance.

In addition, the statistical microhardness analysis revealed the probability distribution of the hardness values, indicating that the sample followed a normal distribution, which suggests that the sample has a homogeneous structure. The Vickers hardness of 3% HEA B_4C ceramic was higher than that of monolithic B_4C.

This study highlights the potential of HEA-doped B_4C for use in environments where both mechanical strength and corrosion resistance are critical factors. Future research lines to further investigate the material's properties and its applications include the following: (1) examining the effects of doping B_4C with elevated concentrations of HEAs (e.g., 4%, 5%, or higher) to find the saturation point or optimal concentration for improved attributes such as corrosion resistance, hardness, toughness, or thermal stability; (2) testing various HEA compositions to determine how specific elements within the HEA affect the properties of B_4C, thereby identifying the HEA composition that provides enhanced corrosion resistance, mechanical, thermal, or electrical properties.

Author Contributions: Conceptualization, A.D.R.-C.; methodology, A.D.R.-C.; software, A.D.R.-C.; validation, A.D.R.-C., B.C.O., J.C.M.-R. and G.G.; formal analysis, A.D.R.-C. and B.C.O.; investigation, A.D.R.-C.; resources, J.C.M.-R. and G.G.; data curation, A.D.R.-C.; writing—original draft preparation, A.D.R.-C.; writing—review and editing, A.D.R.-C.; visualization, A.D.R.-C.; supervision, J.C.M.-R. and G.G. All authors have read and agreed to the published version of the manuscript.

Funding: This research received no external funding.

Data Availability Statement: The original contributions presented in this study are included in the article. Further inquiries can be directed to the corresponding author.

Acknowledgments: We hereby acknowledge the European project 2023-1-RO01-KA220-HED-000159985: Smart Healthcare Engineering and Cabildo of Gran Canaria project with the reference Cabildo22-01.

Conflicts of Interest: The authors declare no conflicts of interest.

References

1. Suri, A.K.; Subramanian, C.; Sonber, J.K.; Ch Murthy, T.S.R. Synthesis and Consolidation of Boron Carbide: A Review. *Int. Mater. Rev.* **2010**, *55*, 4–38. [CrossRef]
2. Pérez, S.; Tamayo, P.; Rico, J.; Alonso, J.; Thomas, C. Effect of Fibers and Boron Carbide on the Radiation Shielding Properties of Limestone and Magnetite Aggregate Concrete. *Prog. Nucl. Energy* **2024**, *175*, 105320. [CrossRef]
3. Tamayo, P.; Thomas, C.; Rico, J.; Pérez, S.; Mañanes, A. Radiation Shielding Properties of Siderurgical Aggregate Concrete. *Constr. Build. Mater.* **2022**, *319*, 126098. [CrossRef]
4. Zhang, W. A Review of Tribological Properties for Boron Carbide Ceramics. *Prog. Mater. Sci.* **2021**, *116*, 100718. [CrossRef]
5. Domnich, V.; Reynaud, S.; Haber, R.A.; Chhowalla, M. Boron Carbide: Structure, Properties, and Stability under Stress. *J. Am. Ceram. Soc.* **2011**, *94*, 3605–3628. [CrossRef]
6. Zorzi, J.E.; Perottoni, C.A.; Da Jornada, J.A.H. Hardness and Wear Resistance of B4C Ceramics Prepared with Several Additives. *Mater. Lett.* **2005**, *59*, 2932–2935. [CrossRef]
7. Ortiz, A.L.; Candelario, V.M.; Moreno, R.; Guiberteau, F. Near-Net Shape Manufacture of B4C–Co and ZrC–Co Composites by Slip Casting and Pressureless Sintering. *J. Eur. Ceram. Soc.* **2017**, *37*, 4577–4584. [CrossRef]
8. Frage, N.; Hayun, S.; Kalabukhov, S.; Dariel, M.P. The effect of Fe addition on the densification of B 4 C powder by spark plasma sintering. *Powder Metall. Met. Ceram.* **2007**, *46*, 533–538. [CrossRef]
9. Ebrahimi, S.; Heydari, M.S.; Baharvandi, H.R.; Ehsani, N. Effect of Iron on the Wetting, Sintering Ability, and the Physical and Mechanical Properties of Boron Carbide Composites: A Review. *Int. J. Refract. Met. Hard Mater.* **2016**, *57*, 78–92. [CrossRef]
10. Larsson, P.; Axéax'axé, N.N.; Hogmark, S. Improvements of the Microstructure and Erosion Resistance of Boron Carbide with Additives. *J. Mater. Sci.* **2000**, *35*, 3433–3440. [CrossRef]
11. Levin, L.; Frage, N.; Dariel, M.P. The Effect of Ti and TiO 2 Additions on the Pressureless Sintering of B 4 C. *Metall. Mater. Trans. A* **1999**, *30*, 3201–3210. [CrossRef]

12. Rodríguez-Rojas, F.; Moreno, R.; Guiberteau, F.; Ortiz, A.L. Aqueous Colloidal Processing of Near-Net Shape B4C-Ni Cermet Compacts. *J. Eur. Ceram. Soc.* **2016**, *36*, 1915–1921. [CrossRef]
13. Cui, G.; Han, B.; Yang, Y.; Wang, Y.; Chunyang, H. Microstructure and Tribological Property of CoCrFeMoNi High Entropy Alloy Treated by Ion Sulfurization. *J. Mater. Res. Technol.* **2020**, *9*, 2598–2609. [CrossRef]
14. Brito-Garcia, S.J.; Mirza-Rosca, J.C.; Jimenez-Marcos, C.; Voiculescu, I. Impact of Ti Doping on the Microstructure and Mechanical Properties of CoCrFeMoNi High-Entropy Alloy. *Metals* **2023**, *13*, 854. [CrossRef]
15. Yang, F.; Wang, J.; Zhang, Y.; Wu, Z.; Zhang, Z.; Zhao, F.; Huot, J.; Grobivć Novaković, J.; Novaković, N. Recent Progress on the Development of High Entropy Alloys (HEAs) for Solid Hydrogen Storage: A Review. *Int. J. Hydrogen Energy* **2022**, *47*, 11236–11249. [CrossRef]
16. Fu, M.; Ma, X.; Zhao, K.; Li, X.; Su, D. High-Entropy Materials for Energy-Related Applications. *iScience* **2021**, *24*, 102177. [CrossRef]
17. Rios, M.L.; Baldevenites, V.L.; Voiculescu, I.; Rosca, J.M. AlCoCrFeNi High Entropy Alloys as Possible Nuclear Materials. *Microsc. Microanal.* **2020**, *26*, 406–407. [CrossRef]
18. Li, T.; Wang, D.; Zhang, S.; Wang, J. Corrosion Behavior of High Entropy Alloys and Their Application in the Nuclear Industry—An Overview. *Metals* **2023**, *13*, 363. [CrossRef]
19. Socorro-Perdomo, P.; Florido-Suarez, N.; Voiculescu, I.; Mirza-Rosca, J. Biocompatibility of New High-Entropy Alloys with Non-Cytotoxic Elements. *Microsc. Microanal.* **2021**, *27*, 1772–1774. [CrossRef]
20. Castro, D.; Jaeger, P.; Baptista, A.C.; Oliveira, J.P. An Overview of High-entropy Alloys as Biomaterials. *Metals* **2021**, *11*, 648. [CrossRef]
21. Zhang, J.; Tse, K.; Wong, M.; Zhang, Y.; Zhu, J. A Brief Review of Co-Doping. *Front. Phys.* **2016**, *11*, 117405. [CrossRef]
22. Dai, C.; Zhao, T.; Du, C.; Liu, Z.; Zhang, D. Effect of Molybdenum Content on the Microstructure and Corrosion Behavior of FeCoCrNiMox High-Entropy Alloys. *J. Mater. Sci. Technol.* **2020**, *46*, 64–73. [CrossRef]
23. Li, Y.; Zhang, J.; Huang, X.; Liu, J.; Deng, L.; Han, P. Influence of Laser Power on Microstructure Evolution and Properties of Laser Cladded FeNiCoCrMo HEA Coatings. *Mater. Today Commun.* **2023**, *35*, 105615t. [CrossRef]
24. Shang, C.; Axinte, E.; Sun, J.; Li, X.; Li, P.; Du, J.; Qiao, P.; Wang, Y. CoCrFeNi(W1 − XMox) High-Entropy Alloy Coatings with Excellent Mechanical Properties and Corrosion Resistance Prepared by Mechanical Alloying and Hot Pressing Sintering. *Mater. Des.* **2017**, *117*, 193–202. [CrossRef]
25. Wu, H.; Zhang, S.; Wang, Z.Y.; Zhang, C.H.; Chen, H.T.; Chen, J. New Studies on Wear and Corrosion Behavior of Laser Cladding FeNiCoCrMox High Entropy Alloy Coating: The Role of Mo. *Int. J. Refract. Metals Hard Mater.* **2022**, *102*, 105721. [CrossRef]
26. Brito-Garcia, S.; Mirza-Rosca, J.; Geanta, V.; Voiculescu, I. Mechanical and Corrosion Behavior of Zr-Doped High-Entropy Alloy from CoCrFeMoNi System. *Materials* **2023**, *16*, 1832. [CrossRef]
27. Semikolenov, A.; Shalnova, S.; Klinkov, V.; Andreeva, V.; Salynova, M.; Larionova, T.; Tolochko, O. Effect of al Content on Phase Compositions of Fenicocrmo0.5alx High Entropy Alloy. *Metals* **2021**, *11*, 1734. [CrossRef]
28. Dai, C.; Luo, H.; Li, J.; Du, C.; Liu, Z.; Yao, J. X-Ray Photoelectron Spectroscopy and Electrochemical Investigation of the Passive Behavior of High-Entropy FeCoCrNiMox Alloys in Sulfuric Acid. *Appl. Surf. Sci.* **2020**, *499*, 143903. [CrossRef]
29. Wang, L.; Mercier, D.; Zanna, S.; Seyeux, A.; Laurent-Brocq, M.; Perrière, L.; Guillot, I.; Marcus, P. Study of the Surface Oxides and Corrosion Behaviour of an Equiatomic CoCrFeMnNi High Entropy Alloy by XPS and ToF-SIMS. *Corros. Sci.* **2020**, *167*, 108507. [CrossRef]
30. Szymczak, T.; Gumienny, G.; Klimek, L.; Goły, M.; Szymszal, J.; Pacyniak, T. Characteristics of Al-Si Alloys with High Melting Point Elements for High Pressure Die Casting. *Materials* **2020**, *13*, 4861. [CrossRef]
31. Rajkumar, V.B.; Du, Y.; Liu, S.; Cheng, K.; Srivastav, A.K. Measurements of the Melting Points, Liquidus, and Solidus of the Mo, Ta, and MoTa Binary Alloys Using a Novel High-Speed Pyrometric Technique. *Int. J. Refract. Metals Hard Mater.* **2020**, *93*, 105335. [CrossRef]
32. Wang, W.; Wang, J.; Sun, Z.; Li, J.; Li, L.; Song, X.; Wen, X.; Xie, L.; Yang, X. Effect of Mo and Aging Temperature on Corrosion Behavior of (CoCrFeNi)100-XMox High-Entropy Alloys. *J. Alloys Compd.* **2020**, *812*, 152139. [CrossRef]
33. Fu, Y.; Huang, C.; Du, C.; Li, J.; Dai, C.; Luo, H.; Liu, Z.; Li, X. Evolution in Microstructure, Wear, Corrosion, and Tribocorrosion Behavior of Mo-Containing High-Entropy Alloy Coatings Fabricated by Laser Cladding. *Corros. Sci.* **2021**, *191*, 109727. [CrossRef]
34. *ASTM G5-94(2004)*; Standard Reference Test Method for Making Potentiostatic and Potentiodynamic Anodic. ASTM International: West Conshohocken, PA, USA, 2004.
35. *ISO 16773-1-4:2016*; Electrochemical Impedance Spectroscopy (EIS) on Coated and Uncoated Metallic Specimens. ISO: Geneva, Switzerland, 2016.
36. *ISO 14577-1:2015*; Metallic Materials—Instrumented Indentation Test for Hardness and Materials Parameters—Part 1: Test Method. ISO: Geneva, Switzerland, 2015.
37. Ocak, B.C.; Goller, G. Investigation the Effect of FeNiCoCrMo HEA Addition on Properties of B4C Ceramic Prepared by Spark Plasma Sintering. *J. Eur. Ceram. Soc.* **2021**, *41*, 6290–6301. [CrossRef]

38. German, R.M.; Suri, P.; Park, S.J. Review: Liquid Phase Sintering. *J. Mater. Sci.* **2009**, *44*, 1–39. [CrossRef]
39. Wagner, C.; Traud, W. "On the Interpretation of Corrosion Processes through the Superposition of Electrochemical Partial Processes and on the Potential of Mixed Electrodes", with a Perspective by F. Mansfeld. *Corrosion* **2006**, *62*, 843–855. [CrossRef]
40. Rico-Cano, A.D.; Mirza-Rosca, J.C.; Ocak, B.C.; Goller, G. Corrosion Behavior of New B4C Ceramic Doped with High-Entropy Alloy in an Aggressive Environment. *Microsc. Microanal.* **2024**, *30*, ozae044.666. [CrossRef]
41. Boukamp, B.A. A Nonlinear Least Squares Fit Procedure for Analysis of Immittance Data of Electrochemical Systems. *Solid State Ion.* **1986**, *20*, 31–44. [CrossRef]
42. Jáquez-Muñoz, J.M.; Gaona-Tiburcio, C.; Méndez-Ramírez, C.T.; Baltazar-Zamora, M.Á.; Estupinán-López, F.; Bautista-Margulis, R.G.; Cuevas-Rodríguez, J.; Flores-De los Rios, J.P.; Almeraya-Calderón, F. Corrosion of Titanium Alloys Anodized Using Electrochemical Techniques. *Metals* **2023**, *13*, 476. [CrossRef]
43. Uzun, A.; Asikuzun, E.; Gokmen, U.; Cinici, H. Vickers Microhardness Studies on B4C Reinforced/Unreinforced Foamable Aluminium Composites. *Trans. Indian Inst. Met.* **2018**, *71*, 327–337. [CrossRef]
44. Cramer, C.L.; Cakmak, E.; Unocic, K.A. Hardness Measurements and Interface Behavior of SiC-B4C-Si Multiple Phase Particulate Composites Made with Melt Infiltration and Additive Manufacturing. *J. Compos. Sci.* **2023**, *7*, 172. [CrossRef]
45. Ma, H.; Liang, Y.; Fu, H. Effect of B4C Addition on Microstructure and Wear Resistance of Laser Cladding NiCrBSi Coatings. *JOM* **2023**, *75*, 515–525. [CrossRef]